Optical Materials 152 (2024) 115557

Contents lists available at ScienceDirect

Optical Materials

journal homepage: www.elsevier.com/locate/optmat

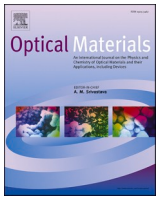

Research Article

Growth and characterization of Fe-doped CuO/ZnO binary oxide thin films for possible optoelectronic applications

Serra Soğan [a], Ersin Yücel [b,*], Ebru Karakaş Sarıkaya [c], Osman Kahveci [d], Raşit Aydın [e], Abdullah Akkaya [f], Bünyamin Şahin [c,g]

[a] Department of Physics, Graduate School of Natural and Applied Sciences, Hatay Mustafa Kemal University, Hatay, Turkey
[b] Department of Physics, Faculty of Arts and Sciences, Hatay Mustafa Kemal University, Hatay, Turkey
[c] Department of Basic Sciences, Faculty of Engineering, Necmettin Erbakan University, Konya, Turkey
[d] Department of Physics, Faculty of Sciences, Erciyes University, Kayseri, Turkey
[e] Department of Physics, Faculty of Sciences, Selçuk University, Konya, Turkey
[f] Mucur Technical Vocational Schools, Tech. Prog. Department, Kırşehir Ahi Evran University, Kırşehir, Turkey
[g] BITAM-Science and Technology Research and Application Center, Necmettin Erbakan University, Konya, Turkey

ARTICLE INFO

Keywords:
Fe-doping
Bandgap
Resistivity
Composite film
Binary oxides

ABSTRACT

Nanoscale binary oxide thin film structures of pristine and Fe-substituted CuO/ZnO have been produced on soda-lime glass substrates by the SILAR method and characterized by different acceptable analytical approaches. The more irregular and lumpy ZnO in the pristine CuO/ZnO binary thin film sample evolved into more regular and hexagonal prismatic structures with the addition of Fe. XRD patterns of the samples indicated that both monoclinic CuO and hexagonal ZnO phases were present without any impurities. Optical analyses by meaning absorbance and transmittance measurements exhibit an important change in the energy band gap and transmittance value with the Fe doping ratio. The energy band edges of the bare sample shift to red with increasing Fe percentage in the starting solution, presumably due to an increase in the carrier concentration. The transfer length method (TLM) is used to define the conductivity properties of the samples, which considers the contact properties and structural features of thin films. The minimum specific contact resistivity of 0.865×10^6 Ω□ was obtained by 3.0 % Fe-implemented CuO/ZnO binary oxide samples, and the addition of Fe increased the effective transfer length of thin films.

1. Introduction

Great progress has been made in the preparation, characterization, and functional applications of various nanomaterials because of the rapid development of nanoscience and nanotechnology over the last few decades [1–3]. Among advanced materials, nanostructured metal oxides (MO) are highly sophisticated materials that have attracted significant interest because of their unique topologies, distinctive properties, and simple, cost-effective, and technologically straightforward production processes. One of the most common categories of compounds on Earth is MO, which comes in various crystalline forms, atomic configurations, and chemical compositions [4–7].

Among the various MOs, zinc oxide (ZnO) possesses unique properties, including high excitation binding energy at room temperature, chemical and thermal stability, n-type semiconductor characteristics, and biocompatibility. ZnO exhibits a broad 3.3 eV direct bandgap and 60 meV excitation binding energy. High temperature stability, strong biocompatibility, an easy etching procedure, a large supply of raw materials, low cost, non-toxicity, and minimal pollution are only a few of the benefits of ZnO [8–10]. Copper oxide (CuO) is another helpful member of the MO family. It has high intrinsic and catalytic capabilities and a low band gap (1.2 eV), which makes it appropriate for photodetector applications. CuO is a naturally abundant, highly stable p-type semiconductor with conductivity of 10^{-4} s/cm. It is also biosafe [11,12].

Nanocomposites (NC) composed of semiconductors or MOs are a significant type of heterogeneous nanostructure. They frequently demonstrate superior physical and chemical properties compared with isolated individual nanoparticles. When two or more fundamental elements are combined, a new material is produced that has characteristics distinct from the constituent parts. NCs often exhibit numerous

* Corresponding author.
E-mail address: eyucel@mku.edu.tr (E. Yücel).

https://doi.org/10.1016/j.optmat.2024.115557
Received 22 February 2024; Received in revised form 16 April 2024; Accepted 19 May 2024
Available online 23 May 2024

advantages over traditional materials, such as increased strength, lower density, and reduced cost [13–16].

Several methods have been used to synthesize CuO/ZnO coupled MO, including co-precipitation, chemical vapor deposition, sol–gel, wet impregnation, thermal decomposition, and successive ionic layer adsorption and reaction (SILAR) [17–21]. Compared with other synthesis techniques, the SILAR method is simple, economical, and the easiest to scale up in industries for producing NC [22,23].

Doping CuO/ZnO with metals such as Er, Dy, Mn, N, and Fe is an effective method for enhancing the material's structural, optical, and electronic properties. This method has generated significant interest in the synthesis and characterization of doped materials for multifunctional purposes [24–27].

Iron (Fe) is a significant element that finds extensive use in the doping of single MOs. The element Fe exhibits two primary oxidation states: Fe^{2+} and Fe^{3+}. In most oxidation states, Fe has unpaired electrons in its d-orbitals. Furthermore, it is worth noting that the ionic radius of Fe corresponds to the ionic radii of Cu^{2+} and Zn^{2+} in oxide form. Therefore, it is anticipated that adding Fe ions to the CuO and ZnO lattices will improve the chemical and physical characteristics of the CuO/ZnO nanocomposite [28–30].

To the best of our knowledge, no studies have been conducted on the impact of Fe as a dopant element on the structural, optical, and electrical properties of CuO/ZnO nanocomposites. In this study, pristine and Fe-doped CuO/ZnO nanocomposites were synthesized using an easy-to-use, reasonably priced SILAR approach. The prepared samples' physical characteristics were examined and are discussed in more depth below.

2. Experimental Details

To obtain a robust composite system, bare and Fe-substituted CuO/ZnO NC binary oxides were deposited on soda-lime glass substrates using the SILAR technique. 50 mL of 0.1 M copper (II) chloride dehydrate and 50 mL of 0.1 M zinc acetate dehydrate salts were dissolved in 100 mL of distilled water to obtain a Zn^{2+} and Cu^{2+}solution. The pH of the prepared solution was approximately 12 by adding ammonium hydroxide, and then the temperature of the prepared bath was adjusted to 355 K and retained stable at this value. For the fabrication of binary oxide structures, the glass substrate was first rinsed in cationic precursor (0.1 $Cl_2CuH_4O_2$ and 0.1 M $C_4H_{10}O_6Zn$) for 20 s to adsorb Zn^{2+} and Cu^{2+} ions, followed by washing in deionized water to remove loosely bound Zn^{2+} and Cu^{2+} ions for 10 s. This process was repeated 14 times to acquire the requested thickness of the CuO/ZnO NC binary oxide films. To examine the impact of Fe^{2+} ions on the main characteristic properties of CuO/ZnO NC binary oxides, two varied ratios (1.0 % and 3.0 %) of Fe^{2+} were applied to the starting bath solution. The same deposition process as above with CuO/ZnO was repeated for Fe-doped CuO/ZnO samples. The fabricated binary oxide samples were annealed in an oven at 250 °C for 30 min. A schematic of the SILAR fabricated procedures is shown in Fig. 1.

The microstructural and surface morphological characteristics of the binary oxide samples were investigated using X-ray diffraction and field emission scanning electron microscopy. Elemental composition and mapping were conducted using an energy-dispersive X-ray spectrometer (EDX). The thickness of the films was measured using the AEP Technology NanoMap 500 LS 3D profilometer by measuring different parts of the samples. The energy band gap and transmittance values were determined using a Jasco V-670 UV–Vis spectrophotometer. The molecular structure of the fabricated materials was investigated by Fourier transform-infrared spectroscopy. Current–voltage measurements (I–V) were performed in the dark using a computer-controlled Wonatech Zive SP1 potentiostat system at 273 K. The conductivity performances of the binary oxide samples were evaluated using the transfer length method (TLM).

3. Results and discussion

The effect of Fe-doping on the surface morphology of CuO/ZnO binary oxide thin film samples was investigated using scanning electron microscopy (SEM). As shown in Fig. 2, images of both bare CuO/ZnO (Fig. 2a) and thin film surfaces doped with Fe at two different ratios (Fig. 2b and c) are presented. In all samples, it is observed that the CuO nanostructure (dark gray) covers the ground like a carpet, whereas the ZnO nanostructures (light gray) form surface protrusions like the patterns of this carpet. In the bare sample shown in Fig. 2a, CuO nanostructures have a tighter and less fluffy morphological structure. ZnO nanostructures are also closer to each other and have oval-like nanotips. In Fe-substituted samples, Fig. 2a and b CuO nanoclusters are fluffier and have a distinct morphology. ZnO nanostructures turned into sharper and more pointed nanotips with the addition of Fe.

It has been reported that the differentiation of ZnO nanotips by doping is attributed to lattice mismatches and that dislocations may form an energetically favorable site for further nucleation and growth of ZnO [31]. The results clearly show that the more irregular and lumpy ZnO in the undoped CuO/ZnO binary thin film sample evolves into more regular and hexagonal prismatic structures with the addition of Fe. Morphologies very similar to those in this study were obtained, and this situation was attributed to the anisotropic growth caused by Fe in the study of Sahai, A. et al. [32]. The effect of Fe doping on the CuO nanostructure is also obvious. The CuO nanostructures changed into a fluffier structure. This change in morphology can provide volumetric

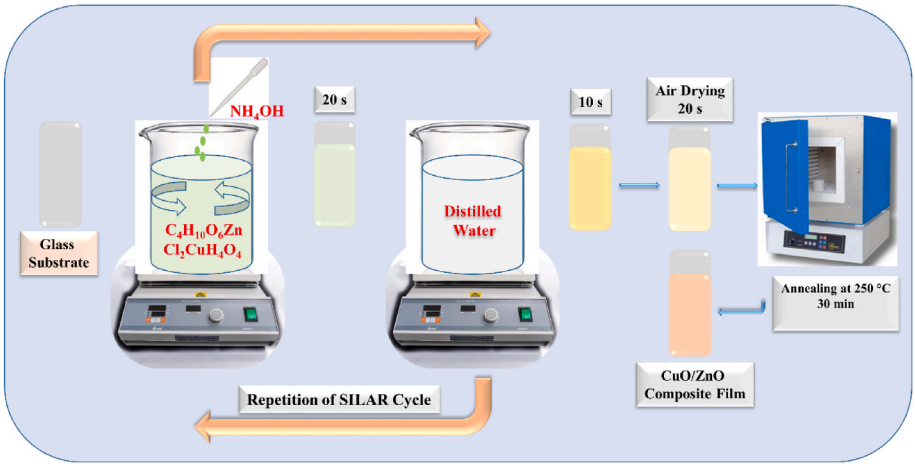

Fig. 1. The schematic exhibition for fabrication of CuO/ZnO NC binary oxides using a SILAR procedure.

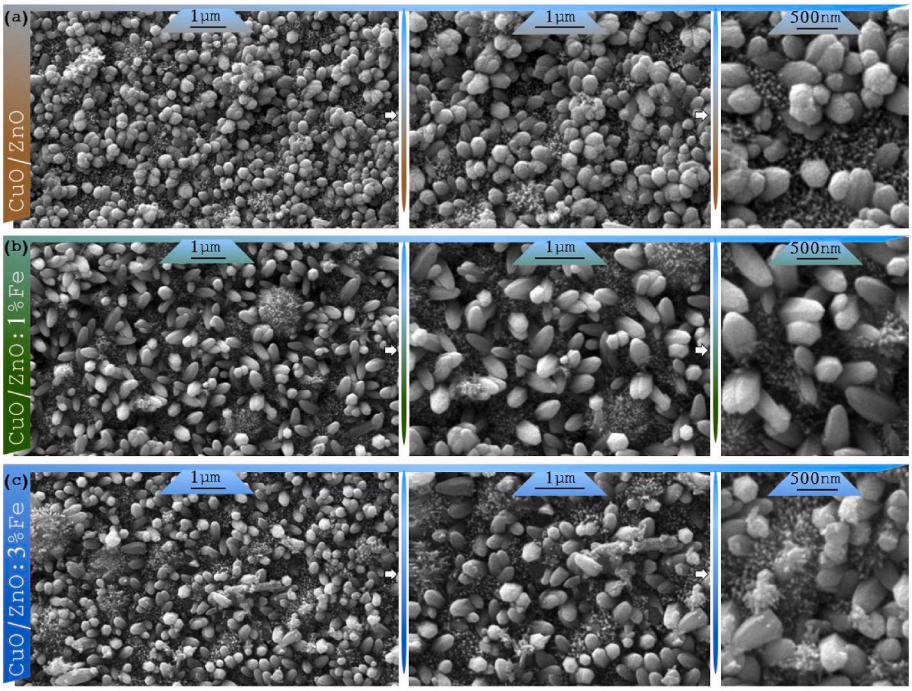

Fig. 2. Typical FE-SEM images of CuO/ZnO binary oxide thin films at different magnifications (scales above the figures): (a) bare CuO/ZnO, (b) 1.0 % Fe-substituted CuO/ZnO, and (c) 3.0 % Fe-substituted CuO/ZnO.

increase on the surface. Chaudhary, M. et al. [33] clearly observed that the morphology of CuO nanostructures changes with the doping of Fe ions in the CuO lattice, which they attributed to the interstitial Fe ions at Cu sites in the CuO lattice. This morphological change is also compatible with our thickness measurements. While the film thickness was 0.33 µm in the undoped CuO/ZnO binary oxide thin film sample, it was measured as 0.67 µm for the 1 % Fe-doped thin film and 1.49 µm for the 3 % Fe-doped thin film. The thickness values of fabricated samples were summarized in Table 1. The results show that the film thickness increased approximately twofold with 1 % Fe doping and more than fourfold with 3 % Fe doping. Taking advantage of pixels' analysis program, the average size of the obtained particles was estimated to check the influence of Fe substitution. The average sizes of the obtained particles are found to be 198.52 and 266.20 nm for bare and 3.0 % Fe-doped composite samples respectively. These findings are consistent with the outcomes by XRD, i.e., the increase of crystallite size with increasing Fe content in the growth bath.

Elemental analyses and surface mapping of the samples were performed using the energy dispersive X-ray spectrometry (EDX) method. The results are shown in Fig. 3a for the undoped CuO/ZnO binary oxide thin film and in Fig. 3b for the CuO/ZnO:1.0%Fe sample with 1.0 % Fe doping. A bar graph showing the percentage composition of the elements by weight is embedded in these figures. Thin film samples were subjected to Au coating to increase conductivity before SEM-EDX analysis. The results were interpreted by excluding the peaks related to the coating from the analysis. In the mapping, Zn is represented by orange, Cu by red, O by green, and the color of Fe, which is the doping element, by cyan. The peaks belonging to the elements forming the thin film and the colors representing the elements in the mapping process were successfully obtained. The cyan color of the doping element Fe is clearly noticeable in maps containing all colors, and in the mapping of Fe alone, it is observed how it is incorporated into the entire structure. Similar peaks were obtained in both analyses, but the Fe peak resulting from doping is seen in Fig. 3b.

Table 1
Relative peak intensity, FWHM, and crystallite size and film thickness of nanostructured CuO/ZnO binary oxide thin films.

Sample Name	Relative peak intensity	FWHM (radian)	Crystallite size (nm)	Film thickness (µm)
	Z(002)			
CuO/ZnO	81100	0.00495	30.63	0.33
1.0 % Fe-doped CuO/ZnO	86950	0.00464	32.63	0.67
3.0 % Fe-doped CuO/ZnO	82133	0.00457	33.18	1.49

In the current study, the crystallite sizes and phase analysis of the CuO/ZnO binary oxide crystalline structures were investigated using X-ray diffraction (XRD) measurements in the scan range of 30° to 80°, as illustrated in Fig. 4.

The XRD results of binary oxide thin films show that the synthesized films have a polycrystalline nature and that the CuO and ZnO diffraction peaks are in good agreement with the JCPDS files (JCPDS card no: 01-075-6445 and JCPDS card no: 00-041-0254). Moreover, the XRD patterns of the samples indicate that both monoclinic CuO and hexagonal ZnO phases are present without any impurities. As can be seen from the XRD spectrum of the CuO/ZnO binary oxide thin films, peaks originating from the diffraction planes (002), (111), (020), (113), and (311) and (100), (002), (101), (102), (110), (103), (112), and (004) are assigned to the CuO and ZnO structures, respectively. This result is consistent with our previously reported results [34]. It can be seen from the XRD pattern of the binary oxide thin films that there are two prominent ZnO peaks at the (002) and (101) planes, which show that the samples have a highly crystalline structure. As tabulated in Table 1, the intensities of the ZnO (002) peaks first increased and then decreased, indicating the presence of Fe^{2+} ions in the CuO/ZnO binary oxide lattice. The justification for the crystallinity quality and structural alteration is the reaction between Cu, Zn and Fe elements throughout the thin film deposition process. The increment or decrement in the peak intensities may be owing to the synergistic impact of Cu, Zn and Fe as a host and dopant elements. Hereafter, it can be concluded that the variation in the Fe content of the growth solution has a considerable impact on the nucleation process and

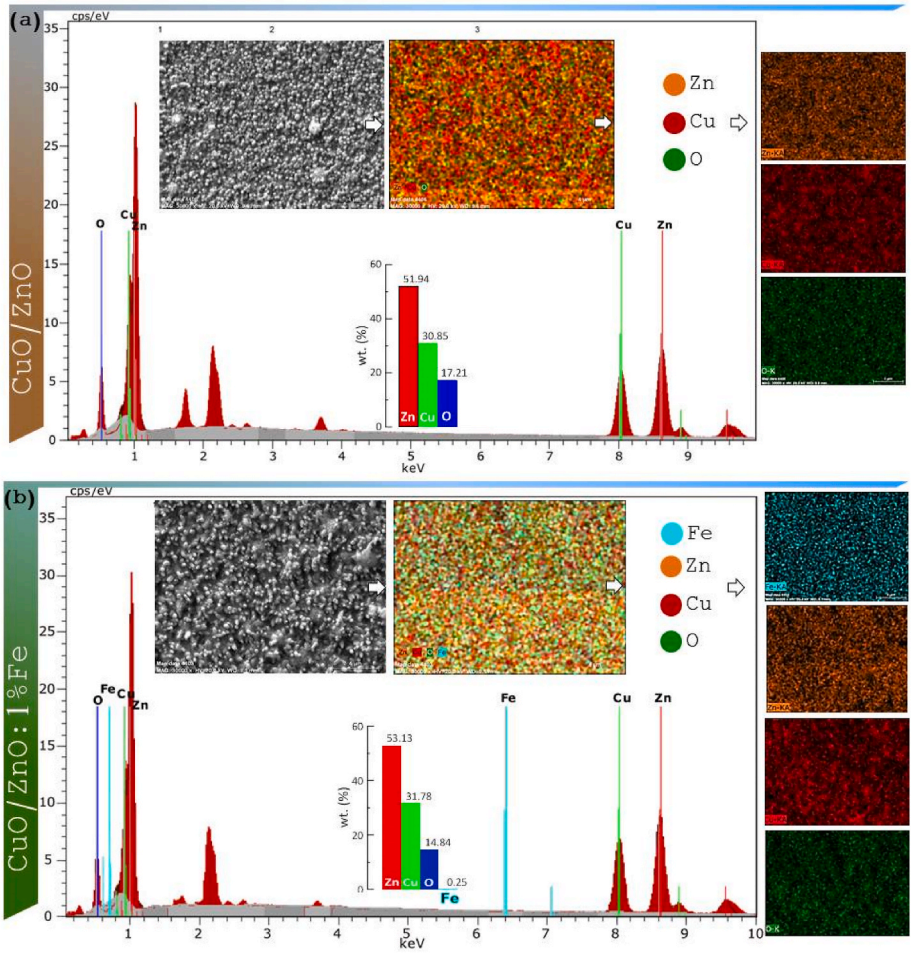

Fig. 3. Elemental composition analysis and EDX mapping results of (a) bare CuO/ZnO and (b) 1.0 % Fe-substituted CuO/ZnO binary oxide samples.

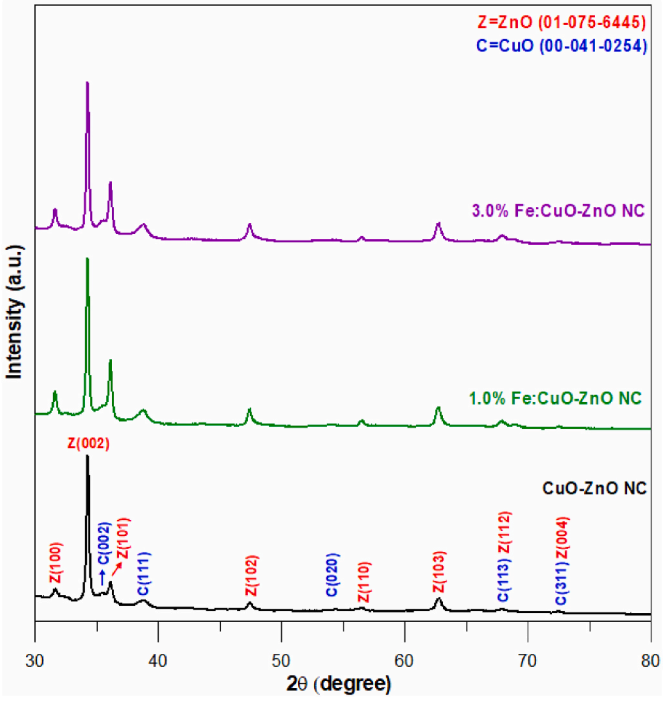

Fig. 4. XRD patterns of the bare CuO/ZnO and Fe-substituted CuO/ZnO binary oxide samples.

crystallinity ability of the ZnO–CuO composite film structure [35,36]. Another reason for this change in the crystallinity quality and structural alteration can be due to the ionic radius distinctions of Cu, Zn, and Fe materials [37,38]. Meantime, the electronegativity properties of Zn, Cu and Fe ions were 1.65, 1.90 and 1.83 respectively. Hence, the Fe dopant atoms can engage the location of Zn and Cu in lattice structure.

When the added in the reaction bath amount of 1.0 % Fe, the highest peak intensity was obtained. Moreover, with increasing iron percentage in the reaction solution, the peak width (FWHM) decreased and the crystallite size increased. The value of D (crystallite size) of the CuO/ZnO binary oxide samples was calculated using the famous Debye–Scherrer equation [39,40]:

$$D = \frac{0.94\lambda}{\beta \cos\theta} \tag{1}$$

where 0.94 is a constant value, the wavelength of the X-ray source is λ, β is the full width at half maximum (FWHM) of the ZnO (002) characteristic peaks and θ is the Bragg's diffraction angle. The most intense diffraction lines (ZnO (002) peaks) were selected to calculate the crystallite size of bare and Fe doped CuO/ZnO binary oxide samples. Table 1 presents the calculated crystallite size values of the CuO/ZnO binary oxide thin films. The alteration of the crystalline quality may be due to the permutation of Fe^{2+} ions into sites in the ZnO and CuO lattice structures during the formation of composite films by the combination of CuO and ZnO. A similar result regarding the increase in crystallite size was found by Sahin et al. [41] and Zaman et al. [42]. The lattice parameters of ZnO hexagonal structure and CuO monoclinic structure were estimated using Eqs. (2) and (3), respectively [43].

$$\frac{1}{d^2}=\frac{4}{3}\left(\frac{h^2+hk+k^2}{a^2}\right)+\frac{l^2}{c^2} \quad (2)$$

$$\frac{1}{d^2}=\frac{1}{sin^2\,\beta}\left(\frac{h^2}{a^2}+\frac{k^2\,sin^2\,\beta}{b^2}+\frac{l^2}{c^2}-\frac{2hlcos\beta}{ac}\right) \quad (3)$$

where d represents an interplanar spacing between the atoms, β represents an inter-axial angle and h, k, l are the Miller indices. The lattice parameters of bare and Fe doped CuO/ZnO binary oxide samples are summarized in Table 2.

The CuO/ZnO binary oxide thin film was analyzed using FTIR spectroscopy to investigate its various vibration modes. The dimensions, morphology, and aggregation state of the nanoparticles affect the modes of FTIR [44]. Fig. 5 displays the FTIR spectra of the Fe-doped and undoped CuO/ZnO binary oxide thin film samples, which were analyzed to confirm their structural properties. The FTIR spectra of the CuO/ZnO binary oxide thin film samples were obtained by recording their vibrational modes in the wavenumber range of 400–4000 cm^{-1}. These spectra, as shown in Fig. 5, revealed the existence of several vibrational modes.

In general, nanostructured metal oxides exhibit prominent absorption peaks in the fingerprint region (below 1000 cm^{-1}) due to stretching vibrations. These vibrations are caused by the interatomic vibration modes of metal oxides. The appearance of broad and intense peaks at around 440 cm^{-1} may be attributed to the combined stretching vibrations of Cu–O and Zn–O bonds [45,46]. In addition, absorption peaks at 679 cm^{-1} and 881 cm^{-1} were identified as characteristic stretching modes of the Cu–O and Zn–O bonds, as demonstrated in Fig. 5. The weak peaks located at 1571 cm^{-1} and 1402 cm^{-1} are ascribed to vibrations of the C═O and –CH_2 bonds, respectively [34]. The presence of absorption peaks around 2350 cm^{-1} may be attributed to the absorption of atmospheric carbon dioxide by metallic cations [47]. Moreover, the presence of water molecules in thin films is responsible for the weak absorption peaks observed at 3728 and 3621 cm^{-1} [48]. Infrared spectroscopy is capable of differentiating FTIR spectra caused by synthesis conditions such as metal/metal ratio, elemental constitution, and the use of a support during the synthesis of the nanoparticle template. The shape and intensity of the absorption bands, as well as the location of the bands at the specified frequencies, provide insights into the vibrational modes of the chemical bonds formed among the pertinent atoms in atomic groups located on the surface of the nanoparticle [49]. The interaction between the dopant ions and host metals could describe the considerable variations in peak intensities across the entire FTIR spectrum [50,51]. The change in the band vibration intensity reveal the incorporation of Fe ion into the ZnO–CuO crystal lattice. The interstitial iron changes the order of the lattice remarkably, which results in the alteration of peak intensity of metal–oxygen vibration frequency in FTIR [52,53].

To explore the optical characteristics of the synthesized binary oxide samples, bare and Fe-doped films were analyzed using a UV–Vis spectrophotometer. The variation in the optical band gap energy values of the thin film samples was calculated using Tauc's equation (Eq. (4)) [54]. The Tauc equation indicates the relationship between photon energy (hυ) and the absorption coefficient (α).

$$(\alpha h\upsilon)=C\left(h\upsilon-E_g\right)^{1/2} \quad (4)$$

Table 2
The lattice parameters of bare and Fe doped CuO/ZnO binary oxide samples.

Sample Name	ZnO (Å) (Hexagonal)		CuO (Å) (Monoclinic)		
	a = b	c	a	b	c
CuO/ZnO	3.2616	5.2185	4.6846	3.4227	5.1316
1.0 % Fe-doped CuO/ZnO	3.2656	5.2294	4.6901	3.4267	5.1375
3.0 % Fe-doped CuO/ZnO	3.2706	5.2318	4.6983	3.4327	5.1466

where C is a constant value and E_g is the optical bandgap energy value. The plots of $(\alpha h\upsilon)^2$ versus hυ of CuO/ZnO binary oxide samples fabricated from pristine and Fe-doped (1.0 % and 3.0 %) samples are displayed in Fig. 6. When Fig. 6 is checked, it is seen that the addition of Fe^{2+} ions into CuO and ZnO lattices decreases the optical band gap value from 1.98 to 1.57 eV. This decrease in the optical band gap might be due to an increase in carrier concentration owing to the successful substitution of Fe^{+2} ions in the ZnO and CuO lattice structures. Additionally, during the formation of CuO/ZnO binary oxide thin films, more reactive sites may be formed that promote electron transfer from ZnO to CuO, which may be the reason for the lower optical band gap for the composite thin film. In addition, alteration in film grain boundaries, changes in structural defects, and crystallinity cause the optical band gap to change [55,56].

The optical transmittance spectra of the fabricated CuO/ZnO binary oxide thin films for bare and different iron doping ratios (1.0 % and 3.0 %) are shown in Fig. 7. The transmittance values of the films decreased from 35.14 to 8.4 % in the 1100 nm region. The film deposited at 3.0 % Fe doping had the lowest transmittance value of 8.4 %. When compared with the 3.0 % Fe-doped thin film, it was observed that the 1.0 % Fe-doped thin film had higher optical transmittance (15.06 % in the 1100 nm region). As a result, the optical transmittance value of the thin films decreased with increasing iron doping ratio. These changes in the optical transmittance of thin films might be linked to the increase in film thickness; at the same time, these changes indicate an increase in the grain size of thin films [56,57]. Both the crystallite size values obtained from the XRD analysis of CuO/ZnO binary oxide thin films and the measured thickness values of thin films confirm these results. In addition, the decrease in optical band gap energy values may also indicate the presence of weak transmittance values for CuO/ZnO binary oxide thin films [58].

The conductivity and contact mechanisms of thin films are quite different from those of bulk materials. While current conduction in bulk materials is more related to bulk properties, current conduction in thin films is related to surface properties rather than bulk properties. For this reason, the transfer length method (TLM), which considers the contact properties and structural features of thin films, such as current crowding, is used for resistance measurements (Fig. 8).

According to this method, multiple (here number of pads was chosen 4) metal contacts were made by thermal evaporation of gold on films with certain distances (d) between each other (see inset in Fig. 9.). Current–voltage (I–V) measurements between the most closed contacts (A and B pads) of bare and Fe-doped CuO/ZnO binary oxide thin films are shown in Fig. 9. All binary oxide thin films showed ohmic behavior, and resistivity depends on the Fe-doping level.

Fig. 10 shows the current–voltage (I–V) evaluation outcomes of 1.0 % Fe-substituted CuO/ZnO binary oxide thin film samples at room temperature. Resistivity values (R_T) were calculated from each I–V measurement and used in d vs. R_T plots Fig. 11. Effective transfer length (L_{eff}) and specific contact resistance (ρ_c) values can be calculated from these plots [59,60].

The slope and intercept of the d vs. R_T plots give the total contact resistance (R_C) and the transfer length (L_T) with the following equations [59]:

$$R_c=\frac{R_{Sk}L_T}{w}\coth\left(d/L_T\right) \quad (5)$$

and

$$L_T=\sqrt{\frac{\rho_c}{R_{Sk}}} \quad (6)$$

Here, w, d and R_{Sk} is the width of the contact, the length of the contact, and the modified sheet resistance under the contact, respectively.

Additionally, under $w\gtrsim 2L_{eff}$ and $2R_{SK}=R_{SH}$ condition, the total

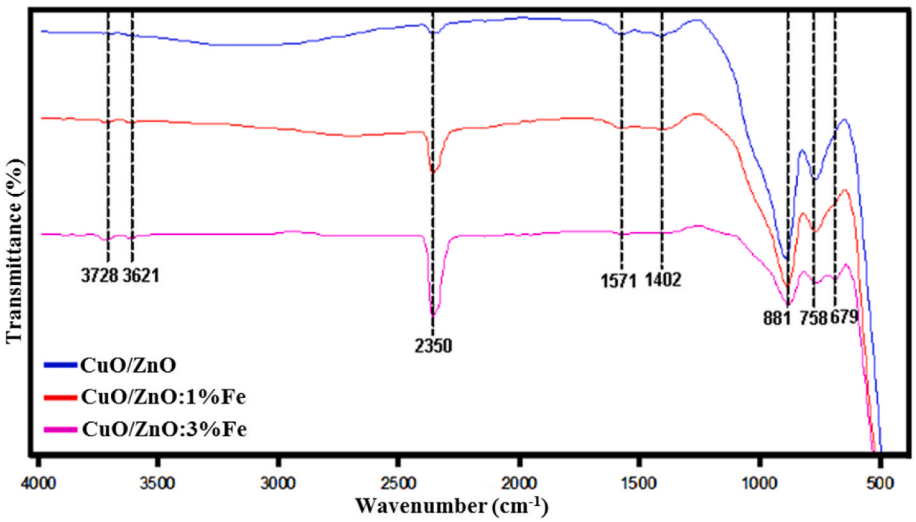

Fig. 5. FTIR spectra of the bare CuO/ZnO and Fe-substituted CuO/ZnO binary oxide samples.

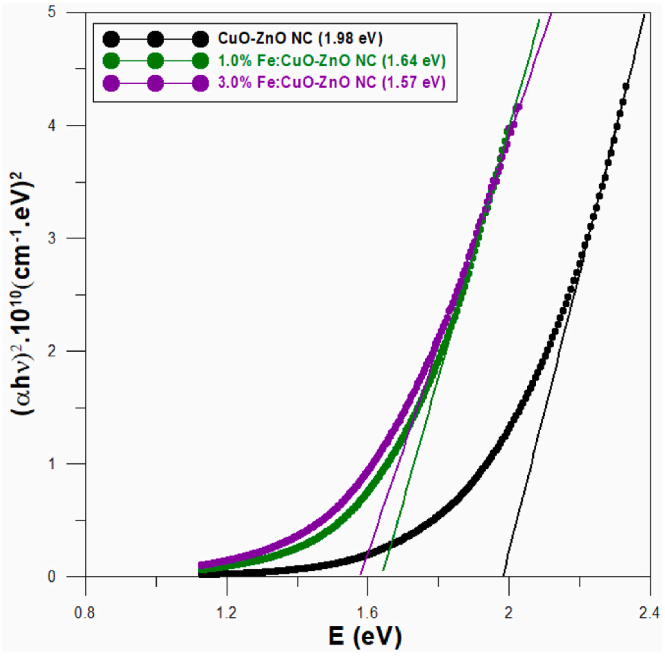

Fig. 6. Plots of $(\alpha h\upsilon)^2$ versus $h\upsilon$ of CuO/ZnO binary oxide thin films prepared bare and Fe-doped (1.0 % and 3.0 %).

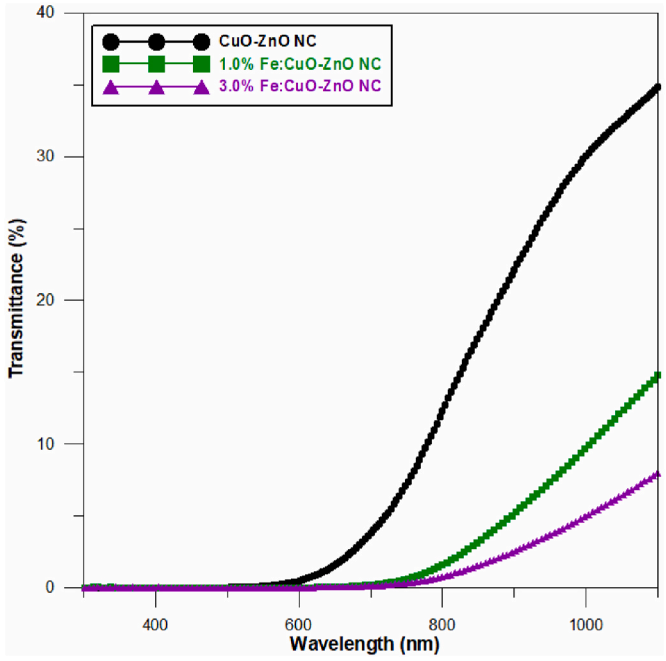

Fig. 7. Optical transmittance spectra of CuO/ZnO binary oxide thin films prepared bare and Fe-doped (1.0 % and 3.0 %).

resistance (R_T) and contact end resistance (R_{end}) are given by the following equations [60,61]:

$$R_T = \frac{2R_{Sk}L_T}{w} + \frac{R_{Sh}l}{w} \tag{7}$$

Written as [60]:

$$R_{end} = \frac{\rho_c}{L_T w} \frac{1}{sinh\left(d/L_T\right)} \tag{8}$$

where R_{Sh} is the sheet resistance of the outside of contact.

R_C, R_{end} and ρ_c, values was slightly decreased with the Fe content (Fig. 12(a–b)). The minimum specific contact resistivity of 0.865×10^6 Ω□ was obtained by 3.0 % Fe-implemented CuO/ZnO binary oxide thin films, and the addition of Fe increased the effective transfer length of thin films. This decrement in contact resistance values may be elucidated by the influence of different parameters such as particle morphology, distribution, and surface roughness [62]. However, as we can see in Table 1, the crystallite size was almost constant and the thickness was remarkably increased with Fe doping. Therefore, the effect of Fe^{+2} ions on conductivity and increment in bulk material under the TLM contacts may cause an increment in specific contact resistivity.

The substitution of appropriate elements in metal-oxide forms can cause varying stages of alterations in the conductivity characteristics of their matrix materials, which are principally affected by the ionic radius, electronegativity, valence state, and bonding energy of the elements with oxygen [[63]. Furthermore, the decreasing value of specific contact resistivity with increasing iron content signs sufficient incorporation of Fe into the interstitial or substitutional sites of both CuO and ZnO lattices [64,65].

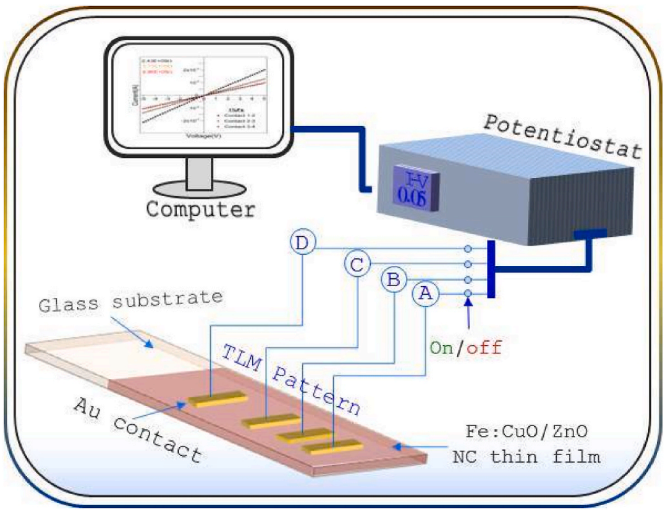

Fig. 8. Schematic representation of the current–voltage (I–V) measurement setup.

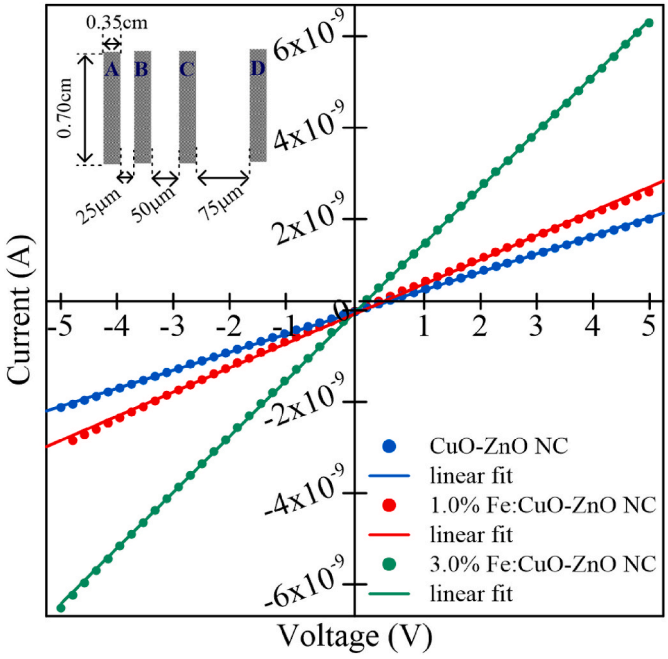

Fig. 9. I–V characteristics between the most closed contacts and the linear fits of the bare CuO/ZnO and Fe-substituted CuO/ZnO binary oxide samples. Inset shows the TLM contact pattern.

4. Conclusion

CuO/ZnO nanocomposite films with different Fe-doping concentrations were successfully synthesized using the SILAR technique. The evolution of CuO and ZnO as distinct phases in each composite was demonstrated by crystal structure studies of bare and doped CuO/ZnO NC. The successful inclusion of Fe ions into the CuO/ZnO lattice was confirmed by shifts in the band gap and the 2-theta angle of the XRD peaks. EDX corroborated the chemical element concentrations and revealed Cu, Zn, O, and Fe in the composites. As the doping weight percentage was increased to 3.0 %, the energy band gap of the CuO/ZnO film was red-shifted from 1.98 to 1.57 eV. 3.0 % Fe-doped CuO/ZnO binary oxide thin films had the lowest specific contact resistivity of $0.865 \times 10^6\ \Omega\square$; the addition of Fe also lengthened the effective transfer length of the thin films. These findings indicate that binary composite

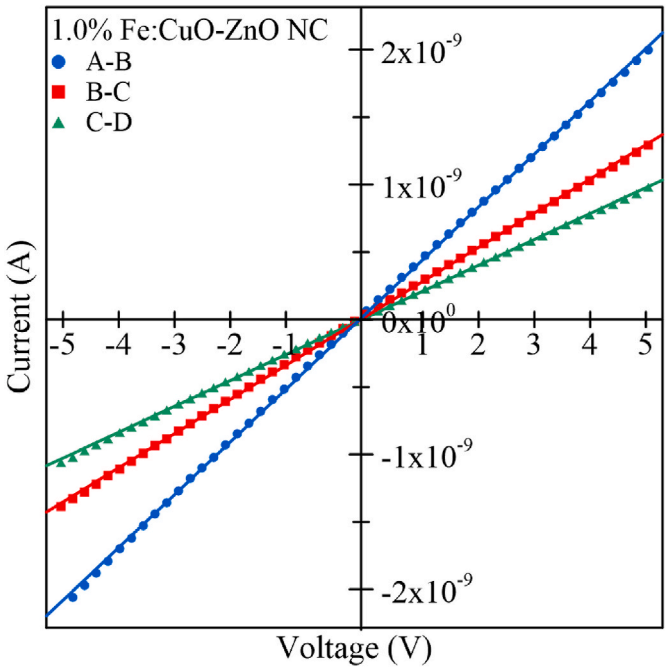

Fig. 10. I–V characteristics of 1.0 % Fe-substituted CuO/ZnO binary oxide thin film sample. The dc resistivity values decreased with pad distance. Inset shows the TLM contact pattern.

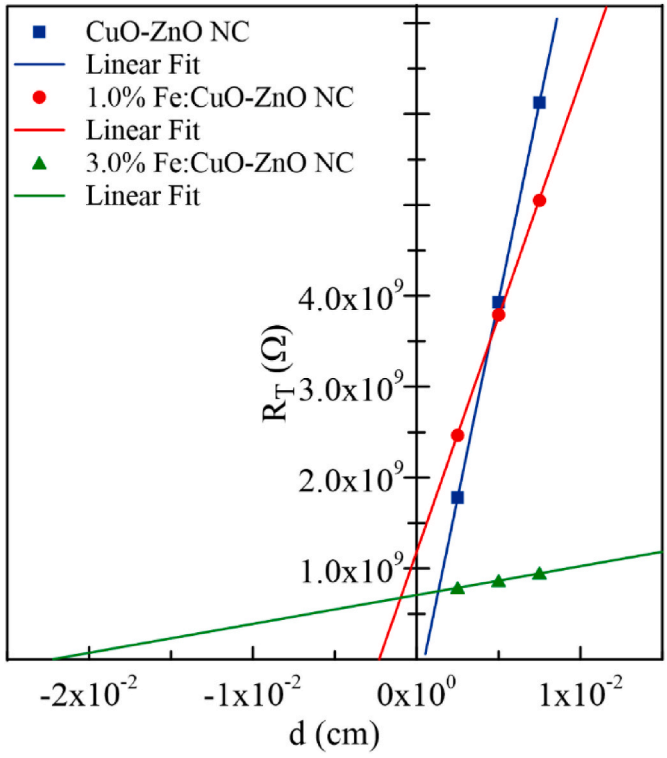

Fig. 11. Total resistance as a function of pad distance plots of bare and Fe-doped CuO/ZnO binary oxide thin films.

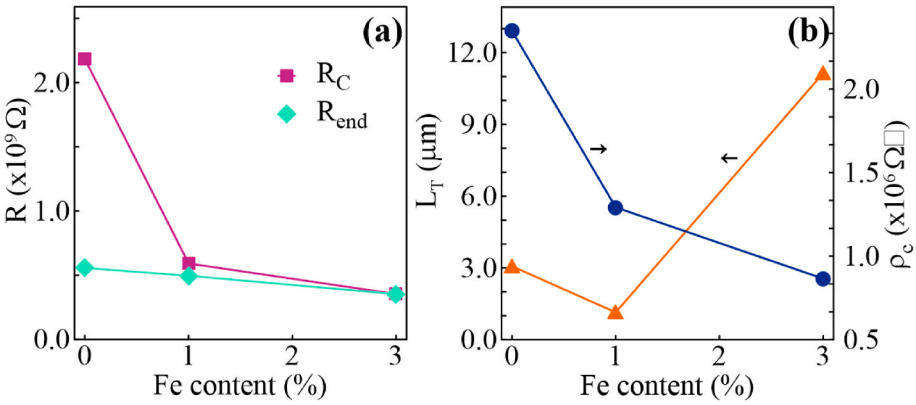

Fig. 12. Contact parameters R_{end}, R_C (a) and ρ_c, L_T (b) as functions of Fe content (%).

forms of CuO/ZnO thin films have potential for use in optoelectronic applications.

CRediT authorship contribution statement

Serra Soğan: Writing – review & editing, Data curation. **Ersin Yücel:** Writing – review & editing, Supervision, Methodology, Investigation, Formal analysis, Data curation. **Ebru Karakaş Sarıkaya:** Writing – review & editing, Data curation. **Osman Kahveci:** Writing – review & editing, Data curation. **Raşit Aydın:** Writing – review & editing, Data curation. **Abdullah Akkaya:** Writing – review & editing, Data curation. **Bünyamin Şahin:** Writing – review & editing, Data curation.

Declaration of competing interest

The authors declare that they have no known competing financial interests or personal relationships that could have appeared to influence the work reported in this paper.

Data availability

The authors do not have permission to share data.

References

[1] T. Tolaymat, A. El Badawy, A. Genaidy, W. Abdelraheem, R. Sequeira, J. Clean. Prod. 143 (2017) 401–412.
[2] A.A. Khan, H.A. Maitlo, I.A. Khan, D. Lim, M. Zhang, K.-H. Kim, J. Lee, J.-O. Kim, Environ. Res. 202 (2021) 111716.
[3] Y.-Y. Liao, Y. Huang, R. Carvalho, M. Choudhary, S. Da Silva, J. Colee, A. Huerta, G.E. Vallad, J.H. Freeman, J.B. Jones, A. Keller, M.L. Paret, Environmental Science & Technology 55 (2021) 13561–13570.
[4] S. Speldrich, M. Wark, G. Wittstock, ACS Appl. Energy Mater. 6 (2023) 9602–9614.
[5] T. Munawar, M.S. Nadeem, F. Mukhtar, M.N.u. Rehman, M. Riaz, S. Batool, M. Hasan, F. Iqbal, Environ. Sci. Pollut. Control Ser. 29 (2022) 90995–91016.
[6] M.Z. Ishaque, Y. Zaman, A. Arif, A.B. Siddique, M. Shahzad, D. Ali, M. Aslam, H. Zaman, M. Faizan, Rsc Adv 13 (2023) 30838–30854.
[7] A. Akkaya, O. Kahveci, R. Aydın, B. Şahin, Appl. Phys. A 127 (2021) 911.
[8] A. Muhammed, T.G. Asere, T.F. Diriba, ACS Omega 9 (2024) 2480–2490.
[9] K. Madi, D. Chebli, H. Ait Youcef, H. Tahraoui, A. Bouguettoucha, M. Kebir, J. Zhang, A. Amrane, Catalysts 14 (2024) 62.
[10] L. Li, Z. Zhang, J. Wang, P. Yang, Mater. Chem. Phys. 291 (2022) 126680.
[11] R. Daira, B. Boudjema, M. Bououdina, M.S. Aida, C.-D. Constantinescu, Influence of Al doping on the physical properties of CuO thin films, Appl. Sci. (2023).
[12] G.p. Singh, K.J. Singh, K. Chandel, P. Kaur, J. Kaur, Inorg. Chem. Commun. 157 (2023) 111250.
[13] Y.J. Leng, S.H. Chan, Electrochem. Solid State Lett. 9 (2006) A56.
[14] S. Haq, M. Rashid, F. Menaa, N. Shahzad, M. Imran Shahzad, S.Y.M. Alfaifi, O. Madkhali, M.D. Aljabri, M. Ashravi, R.A. Tayeb, M.M. Rahman, Arab. J. Chem. 16 (2023) 104917.
[15] C.-C. Lin, S.-E. Chiang, J.-R. Wu, Y.-C. Huang, S.H. Chang, J Alloy Compd 970 (2024) 172274.
[16] H.Z. Asl, S.M. Rozati, J. Alloys Compd. 928 (2022) 167211.
[17] T. Jan, S. Azmat, Q. Mansoor, H.M. Waqas, M. Adil, S.Z. Ilyas, I. Ahmad, M. Ismail, Microb. Pathog. 134 (2019) 103579.
[18] M.A. Khan, N. Nayan, M.K. Ahmad, S.C. Fhong, M.S. Mohamed Ali, M.K. Mustafa, M. Tahir, Opt. Mater. 117 (2021) 111132.
[19] J. Liu, Y. Chen, H. Zhang, Study of highly sensitive formaldehyde sensors based on ZnO/CuO heterostructure via the sol-gel method, Sensors (2021).
[20] W. Ahmad, U. Mehmood, A. Al-Ahmed, F.A. Al-Sulaiman, M.Z. Aslam, M.S. Kamal, R.A. Shawabkeh, Electrochim. Acta 222 (2016) 473–480.
[21] M. Mahdavi, H. Farrokhpour, M. Tahriri, Journal of Thermal Analysis and Calorimetry 132 (2018) 879–893.
[22] H. Safdar, R. Aydın, B. Şahin, Ceram. Int. 48 (2022) 26678–26688.
[23] R. Saad, A.M. Ahmed, K. Abdelkarem, M. Zayed, Z.M. Faidey, G.M. Al-Senani, M. Shaban, M.T. Tammam, H. Hamdy, SILAR-deposited CuO nanostructured films doped with zinc and sodium for improved CO2 gas detection, Nanomaterials (2023).
[24] A. Srivastava, S. Jit, S. Tripathi, IEEE Electron. Device Lett. 42 (2021) 1802–1805.
[25] M. Poloju, N. Jayababu, M.V. Ramana Reddy, Mater. Sci. Eng., B 227 (2018) 61–67.
[26] S.M. Yakout, A.M. El-Sayed, Adv. Powder Technol. 30 (2019) 2841–2850.
[27] S. Rahemi Ardekani, A. Sabour Rouhaghdam, M. Nazari, Chem. Phys. Lett. 705 (2018) 19–22.
[28] M. Salem, J. Salem, H. Ghannam, I. Massoudi, F. Bourguiba, M. Gaidi, J. Mater. Sci. Mater. Electron. 34 (2023) 332.
[29] R. Gupta, N.K. Eswar, J.M. Modak, G. Madras, Catal. Today 300 (2018) 71–80.
[30] S. Schröder, N. Ababii, O. Lupan, J. Drewes, N. Magariu, H. Krüger, T. Strunskus, R. Adelung, S. Hansen, F. Faupel, Mater. Today Chem. 23 (2022) 100642.
[31] J. Wang, H.-f. Luo, T. Chen, Z.-h. Yuan, Nanotechnology 21 (2010) 505603.
[32] A. Sahai, Y. Kumar, V. Agarwal, S.F. Olive-Méndez, N. Goswami, J. Appl. Phys. (2014) 116.
[33] M. Chaudhary, M. Singh, A. Kumar Prachi, Y.K. Gautam, A.K. Malik, Y. Kumar, B. P. Singh, Ceram. Int. 47 (2021) 2094–2106.
[34] O. Kahveci, A. Akkaya, E. Yücel, R. Aydın, B. Şahin, Ceram. Int. 49 (2023) 16458–16466.
[35] A. Taşer, M.E. Güldüren, H. Güney, Mater. Chem. Phys. 272 (2021) 124993.
[36] R.H. Alshammari, M. Aadil, T. Kousar, U. Maqbool, Z. Ahmad, A.M. Alswieleh, T. S. Algarni, M. Naeem, Opt. Mater. 144 (2023) 114314.
[37] N.D.M. Said, M.Z. Sahdan, N. Nayan, H. Saim, F. Adriyanto, A.S. Bakri, M. Morsin, Rsc Adv 8 (2018) 29686–29697.
[38] N.S. Kirik, B. Şahin, Micro and Nanostructures 167 (2022) 207290.
[39] G. Yıldırım, E. Yücel, J. Mater. Sci. Mater. Electron. 33 (2022) 19057–19070.
[40] P. Scherrer, Ges Wiss Göttingen 26 (1918) 98–100.
[41] B. Şahin, A. Acar, T. Kaya, Ceram. Int. 47 (2021) 11405–11414.
[42] Y. Zaman, M.Z. Ishaque, K. Waris, M. Shahzad, A.B. Siddique, M.I. Arshad, H. Zaman, H.M. Ali, F. Kanwal, M. Aslam, M. Mustaqeem, Arab. J. Chem. 16 (2023) 105230.
[43] D. Saravanakkumar, S. Sivaranjani, K. Kaviyarasu, A. Ayeshamariam, B. Ravikumar, S. Pandiarajan, C. Veeralakshmi, M. Jayachandran, M. Maaza, J. Semiconduct. 39 (2018) 033001.
[44] P. Sable, N. Thabet, J. Yaseen, G. Dharne, Trends in Sciences 19 (2022) 3092.
[45] Z.R. Khan, M.S. Khan, M. Zulfequar, M.S. Khan, Mater. Sci. Appl. 2 (2011) 340–345.
[46] P. Mahajan, A. Singh, S. Arya, J Alloy Compd 814 (2020) 152292.
[47] K.H.K.Y.J. Kwon, C.S. Lim, K.B. Shim, J. Ceram. Process. Res. 3 (2002) 146–149.
[48] D. Saravanakkumar, H.A. Oualid, Y. Brahmi, A. Ayeshamariam, M. Karunanaithy, A.M. Saleem, K. Kaviyarasu, S. Sivaranjani, M. Jayachandran, OpenNano 4 (2019) 100025.
[49] I. Markova, I. Zahariev, V. Milanova, D. Ivanova, M. Piskin, L. Fachikov, E. Hristoforou, Rev. Adv. Mater. Sci. 52 (2017) 70–81.
[50] Q.A. Alsulami, A. Rajeh, Opt. Mater. 123 (2022) 111820.
[51] R. Aydın, A. Akkaya, O. Kahveci, B. Şahin, ACS Omega 8 (2023) 20009–20019.
[52] B. Zhang, Y. Tian, J. Zhang, W. Cai, J. Mater. Sci. 46 (2011) 1884–1889.
[53] S. Muthukumaran, M. Ashok kumar, Mater. Lett. 93 (2013) 223–225.
[54] Y. Yücel, Ö. Otuzbir, E. Yücel, Mater. Today Commun. 34 (2023) 105101.
[55] A. Virdian, S. Muhammady, M.A. Naradipa, R. Widita, A. Rusydi, Y. Darma, Ceram. Int. 46 (2020) 27110–27118.

[56] A.M.M. Musa, M. Rasadujjaman, M.A. Gafur, A.T.M.K. Jamil, Thin Solid Films 773 (2023) 139838.
[57] C. Mrabet, R. Jaballah, N. Mahdhi, A. Boukhachem, M. Amlouk, J Alloy Compd 968 (2023) 172252.
[58] E. Yücel, Superlattice. Microst. 135 (2019) 106287.
[59] H. Murrmann, D. Widmann, IEEE Trans. Electron. Dev. 16 (1969) 1022–1024.
[60] D.K. Schroder, Semiconductor Material and Device Characterization, John Wiley & Sons, New York, 2006.
[61] G.K. Reeves, H.B. Harrison, Ieee Electr Device L 3 (1982) 111–113.
[62] R. Aydın, A. Akkaya, B. Şahin, J. Mater. Sci. Mater. Electron. 33 (2022) 23806–23820.
[63] J. Lin, R. Liang, H. Tan, J. Peng, P. Huang, J. Dai, Y. Li, J. Chen, H. Xu, P. Xiao, Thin Solid Films 787 (2023) 140139.
[64] M.M. Ali, M.H. Kabir, M.S. Rahman, Opt. Mater. 148 (2024) 114949.
[65] H. Satılmış, M. Acar, R. Aydın, A. Akkaya, O. Kahveci, B. Şahin, E. Ayyıldız, Opt. Mater. 148 (2024) 114851.